

Image Simulation and Surface Reconstruction of Undercut Features in Atomic Force Microscopy

Xiaoping Qian¹, John Villarrubia², Fenglei Tian¹, Ronald Dixon²

¹ Mechanical and Aerospace Engineering, Illinois Institute of Technology, Chicago, IL 60613

² National Institute of Standards and Technology, Gaithersburg, MD 20899*

ABSTRACT

CD-AFMs (critical dimension atomic force microscopes) are instruments with servo-control of the tip in more than one direction. With appropriately “boot-shaped” or flared tips, such instruments can image vertical or even undercut features. As with any AFM, the image is a dilation of the sample shape with the tip shape. Accurate extraction of the CD requires a correction for the tip effect. Analytical methods to correct images for the tip shape have been available for some time for the traditional (vertical feedback only) AFMs, but were until recently unavailable for instruments with multi-dimensional feedback. Dahlen et al. [J. Vac. Sci. Technol. B23, pp. 2297-2303, (2005)] recently introduced a swept-volume approach, implemented for 2-dimensional (2D) feedback. It permits image simulation and sample reconstruction, techniques previously developed for the traditional instruments, to be extended for the newer tools. We have introduced [X. Qian and J. S. Villarrubia, *Ultramicroscopy*, in press] an alternative dixel-based method, that does the same in either 2D or 3D. This paper describes the application of this method to sample shapes of interest in semiconductor manufacturing. When the tip shape is known (e.g., by prior measurement using a tip characterizer) a 3D sample surface may be reconstructed from its 3D image. Basing the CD measurement upon such a reconstruction is shown here to remove some measurement artifacts that are not removed (or are incompletely removed) by the existing measurement procedures.

Keywords: Dilation, erosion, mathematical morphology, atomic force microscopy, scanning probe microscopy, critical dimension, image reconstruction, metrology

1. INTRODUCTION

The atomic force microscope (AFM) provides an important tool for dimensional measurement of topographic features at atomic resolution. Conventional AFMs, due to their cone-like probe shape and the unidirectional feedback systems, have their images restricted to shapes (called “umbras”) characterized by a single height at each lateral position. Reentrant, or even nearly vertical, parts of specimens are not imaged accurately.

For a number of years now, probes with lateral protrusions and feedback systems with bi-directional servo control have been incorporated into the newer AFM instruments. These instruments, which are capable of imaging undercut features, have found applications as reference metrology tools at SEMATECH and in a number of fabrication facilities. To take full advantage of the hardware capabilities, appropriate image analysis algorithms are required. Until recently, the state of data analysis was as follows:

- Algorithms were based on grayscale morphology with the assumption of an umbra specimen shape. That is they assumed surfaces could be represented as single-value functions. However, reentrant surfaces possess multiple z values for a given (x,y) coordinate and thus cannot be represented by such functions.
- For samples that are not single-valued, the typical procedure to correct for the tip effect was to subtract a constant offset that corresponds to the overall tip width [1]. When appropriate, such as for sloped sidewalls, a correction might also be made for the effect of the vertical offset height of the tip flare. This was typically done by scanning an undercut characterizer to estimate the offset height and using

* Contributions of the National Institute of Standards and Technology are not subject to copyright.

the image to estimate the sidewall slope of the feature and performing an extrapolation to correct the resulting width bias [2,3]. These methods did not generate a reconstructed profile of the surface, but only attempt to correct the effect of the tip on a specific measurand. However, these methods are less effective on complex and irregular structures where simplified models are inappropriate.

This situation changed with the introduction by Dahlen et al. [4] of two approaches to a more complete reconstruction. One is a slope-matching technique. The other is billed by the authors as an “erosion” algorithm (quotes in original) that “is not a direct application of erosion in a strict sense” because it obtains the outer boundary of a surface rather than a complete set of points describing the region. It appears to be a swept volume subtraction method applied to the image surface to reconstruct the sample. It was implemented for 2-dimensional (2D) profiles and demonstrated [4] on these to give good agreement with SEM cross sections. The method should be extendable to 3D. It appears to us that Dahlen’s method is a legitimate implementation of erosion for the surfaces that it treats.

We have also recently introduced an approach to this kind of data analysis, implemented for use in 3D[5]. It is based on an object representation for 3D objects in which the usual rectangular array of pixels (single height) is replaced by an array of “dexels”. Unlike a pixel, a dixel element may have multiple heights in each column. This allows the under-cut features to be represented in the dixel form. We have developed algorithms for dilation and erosion of dexels. These permit image simulation and surface reconstruction for 3D objects of arbitrary shape. The implementation is capable of AFM image simulation and surface reconstruction for complex 3D structures with under-cut features. In this paper we will apply the method to several example problems of interest in semiconductor electronics applications, and show how it corrects various dimensional biases induced by the tip effects.

If the method of Dahlen et al. and the method we present here are both correctly implemented, they should yield the same results. The main distinguishing features of the present work are: 1) The dixel method is a rigorous implementation of set theoretic operators. Because of this we can be certain that the theorems of set theory and mathematical morphology apply to them. This allows relatively easy building up of more complex operations out of simple ones. Indeed, the next items are two such extensions, already made: 2) The present implementation is not limited to erosion alone, but as mentioned above includes dilation, union, intersection, and other set operations. 3) The present implementation is already extended to 3D.

The validity of the developed dilation and erosion algorithms is here demonstrated for structures with and without undercut features. Through the comparison between the new dixel-based software and existing grayscale morphology software, we demonstrate the consistency between the software for structures without under-cut features. Through examples of dilation and erosion operations on a set of known 3D surface shapes, we illustrate the usefulness of the dixel-based software for objects with under-cut surfaces.

In Section 2, we review the key dixel-related concepts underlying the new software presented in [5]. We then present a set of examples that demonstrate the new capabilities of this software in Section 3 and describe how these new capabilities enable the correction of various dimensional biases in Section 4. We conclude this paper in Section 5.

2. DEXEL BASED MATHEMATICAL MORPHOLOGY

The relationship between the sample S , tip T , and image I (apart from ideally small effects due to noise, cantilever twisting, etc.) can be written as

$$I = S \oplus P \quad (1)$$

where $P = -T$ is the reflection of the tip through the origin. (See e.g., [6, 7] and references therein.) The operator in this equation is dilation. Sample reconstruction is by erosion:

$$S_r = I \ominus P \quad (2)$$

A similar equation governs tip reconstruction if a known sample (a tip characterizer) is used. The reconstructed sample, S_r , represents the smallest outer bound on the sample that one is entitled to conclude from a given tip based upon information in the image. It is not in general everywhere equal to S because there may be parts of the sample (e.g., a crevice) not entirely accessible to the tip.

In order to facilitate subsequent discussion, this section reviews the dixel concept and briefly outlines its use in [5] to implement mathematical morphology for general 3D objects.

2.1. Dixel-based representation

The dixel approach is a version of volumetric data representation where 3D objects are represented as a set of 1D blocks with depth on a grid.

We may construct a dixel object, A_d , associated with a real object A , as follows. First choose an origin and orientation for a rectangular coordinate system. Define a grid in the x - y plane of this coordinate system. The x coordinates in this grid are given by $x_i = x_0 + i d_x$ for $i = 0, 1, \dots, m_x - 1$ with i an integer index, m_x the number of grid elements in the x direction, x_0 the position of the first such element, and d_x the grid spacing in the x direction. The y coordinates are similarly defined. Now imagine a line, L_{ij} (with z ranging from $-\infty$ to ∞) at x_i, y_j for each i, j in the grid. We can define A_d as

$$A_d = \bigcup_{i,j} (L_{ij} \cap A) \quad (3)$$

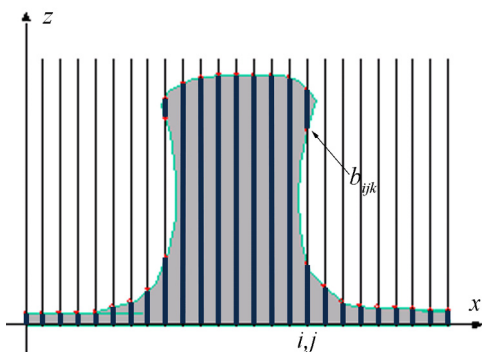


Figure 1 Dixel representation of an object, reproduced from Ref. [5] with permission.

directionality, Boolean simplification, rigid

Here the symbols \cup and \cap represent set union and intersection respectively. A 2D example of this is shown in Figure 1. The object (shown gray) has undercut edges. Those intervals of the lines that are enclosed by the object (i.e., the intersection between the object and the vertical lines) are shown darker. The dixel object representation includes the collection of locations of the endpoints of these intervals in an indexed grid. Each column in the object is represented by a single dixel. The entire object is then a 2D array of dexels.

Formal representation properties of dixel, as noted in [8], include spatial addressability and spatial hashing, motion, discrete translations, null-set representation, and

completeness.

2.2. Set and morphology operations on dixel-represented objects

We build the set and morphological operations on a few primitive operations: dixel *complement*, dixel *union* and block-block *dilation*. All other set operations such as intersection and subtraction, and dilation and erosion operations between dixel objects are derived from these three.

The data representation for each dixel consists of a flag and a linked list of zero or more heights. The flag may take on two values, “inside” or “outside”. The value of this flag indicates whether the starting position at $z \rightarrow -\infty$ is inside or outside the dixel. The heights in the height list are ordered from smallest to largest. The sense of inside/outside toggles back and forth at each height.

Dixel complement: The complement of a set, A , is the set of everything not in A . When A is the set of points contained inside of a shape, as in our current application, its complement is the same shape, but with inside and outside reversed. The dixel complement is accomplished by toggling the value of the dixel flag. Since the sense of inside/outside toggles at each boundary this changes all inside-outside transitions into outside-inside transitions and vice versa.

Dixel-dixel union: A simple model of dixel-dixel union is illustrated in Figure 2. Imagine the two dexels, A and B positioned side by side as shown. Let the “depth” inside A at position z be 1 if z is contained in A and 0 otherwise. The depths inside A and B are “projected” onto the screen at the right, which records their sum. The sum may be 0, 1, or 2. Obviously the depth inside $C = A \cup B$ must be 0 when the depth on the

screen is 0 (z is outside both A and B) and 1 otherwise (i.e., when the total depth is 1 or 2, indicating z is inside one or both of A and B). Changes in the total depth obviously can only happen at the z values in the height lists of A and B .

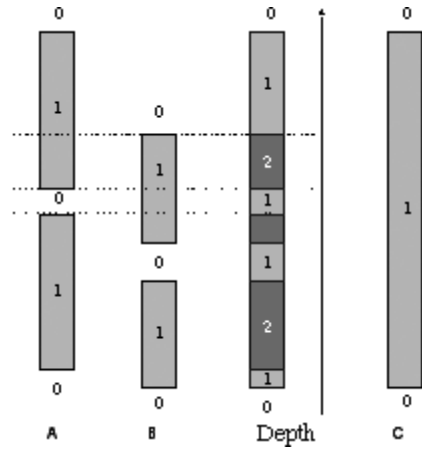


Figure 2 Dixel-dixel union through keeping track of inside/outside status change, reproduced from Ref. [5] with permission.

Block-block dilation Each dixel can be thought of as the union of a number of intervals, or “blocks,” each of which is specified by its lower and upper boundaries. One of these blocks is labeled in Fig. 1. In terms of these blocks the dixel object, A_d , defined in Eq. (3) can also be written as

$$A_d = \bigcup_{i,j} \bigcup_k b_{ijk} \quad (4)$$

where i and j are the grid indices, and k indexes the blocks within each dixel. Dilation of the individual blocks is a particularly simple operation (Figure 3). Dilation translates (or sweeps) one object by all vectors contained in the other, so if $[a,b]$ is a block with lower height boundary at a and upper at b (the left block in the figure), then $[a,b] \oplus [c,d] = [a+c, b+d]$ as shown.

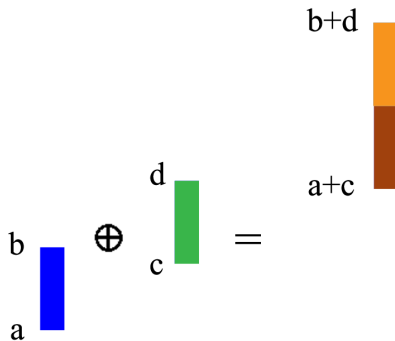


Figure 3 Block-block dilation. Blocks have height but no width—the width shown here is for illustrative purposes only.

Set operations on objects comprised of dexels

The above primitive operators can be used in combination to generate operators for dixel represented objects. Reflection, complement, union, intersection and subtraction are straightforward. They also form the basis of two algorithms that will be directly applied for AFM image simulation and surface reconstruction: dilation and erosion.

Dilation may be implemented in steps. Since the dilation primitive defined above is for block-block dilation, the first (and only new) step is to implement dilation of two dexels. We can think of a dixel as a union of blocks so that if a dixel D has n blocks and \mathcal{D} has m

$$\begin{aligned} D &= \bigcup_{i=1}^n D_i \\ \mathcal{D} &= \bigcup_{j=1}^m \mathcal{D}_j \end{aligned} \tag{5}$$

$D_i, i=1, \dots, n$ are D 's blocks and similarly for \mathcal{D} . It is a general property of dilation that

$$(A \cup B) \oplus C = (A \oplus C) \cup (B \oplus C) \tag{6}$$

See for example Ref. [9] proposition 15. Using this rule, the dilation of dexels D and \mathcal{D} defined by Eq. (5) can be written as the union of dilations of blocks.

$$D \oplus \mathcal{D} = \bigcup_{i=1}^n D_i \oplus \bigcup_{j=1}^m \mathcal{D}_j = \bigcup_{i,j} (D_i \oplus \mathcal{D}_j) \tag{7}$$

where the final union is over all pairings of blocks in the two dexels. The dilations on the right side of Eq. (7) are all instances of the previously defined block-block dilation primitive, and unions of blocks are a special case of the union of dexels primitive. Hence Eq. (7) defines dixel-dixel dilation in terms of operations we already know how to do.

The erosion operation between two dixel objects can be expressed in terms of dilation and complements using the dilation/erosion duality property (Ref. [9] Theorem 25):

$$A \ominus B = [A^c \oplus (-B)]^c \tag{8}$$

In this way we avoid the need to write a separate erosion operator.

3. EXAMPLES

The examples below demonstrate the new capabilities in AFM image simulation and surface reconstruction afforded by the dixel representation in processing undercut structures. As reported in [5], the software has produced identical results on umbra class of 3D objects as existing grayscale mathematical morphology software.

3.1. Image simulation and surface reconstruction for profiles with undercuts

The new method is applicable to AFM imaging of arbitrary 2D profiles of vertical sidewalls and undercut features with a variety of probe shapes. Some of the common tip shapes reported in the literature for imaging sidewalls include parabolic shape [6], three-point [10], flare boot-shaped [1], and elliptical shapes [2, 3, 4].

Example 1 and 2 We used our new dixel-based software to simulate the use of these four probes shapes to image structures of vertical sidewall with round corner in Figure 4, and undercut structure in Figure 5. In these examples, the image simulation is based on dilation and the surface reconstruction is based on erosion. In each of the example, the surfaces and the tips are represented with dixel spacing of 1 nm. The surface contains 500 dixel units. The parabolic tip contains 30 dixel units, the three point one contains 50, and the flared tips both contain 80. We chose the nanometer scale of the simulation for verisimilitude. The use of common shapes reported in the literature is meant to demonstrate the concreteness and realism of the new software. The software itself can model surfaces and tips of any arbitrary shape.

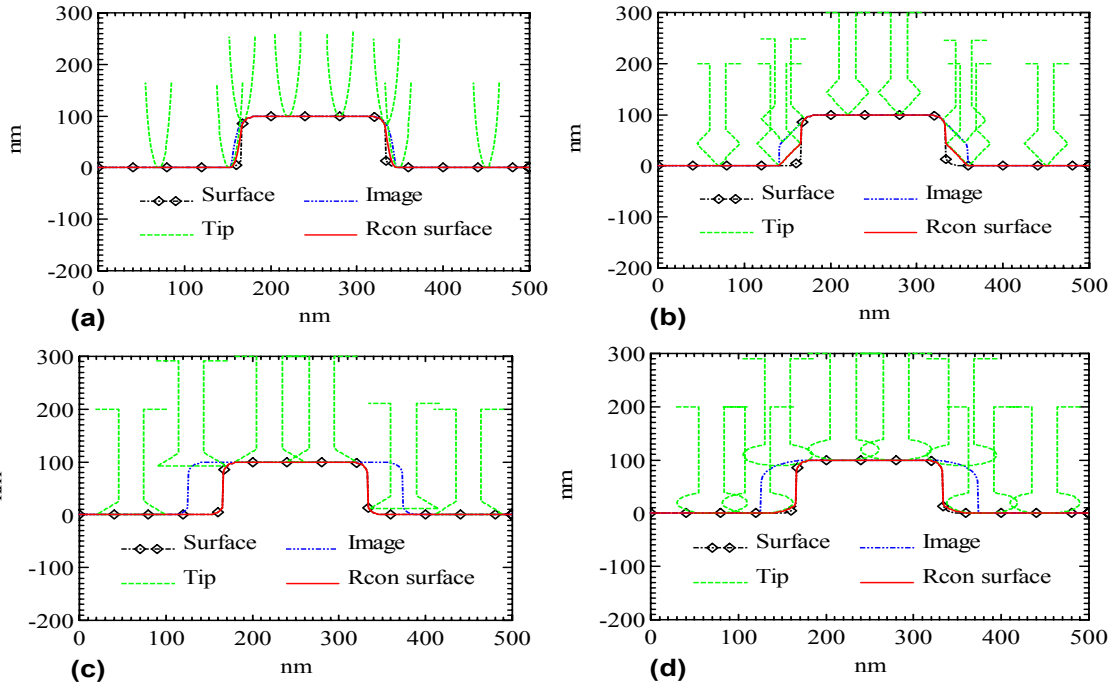


Figure 4 Dilation and erosion on vertical sidewalls with round corners by various tips: parabolic tip in (a), three-point tip in (b), sharp flare-shape tip in (c), and elliptical flare-shape tip in (d).

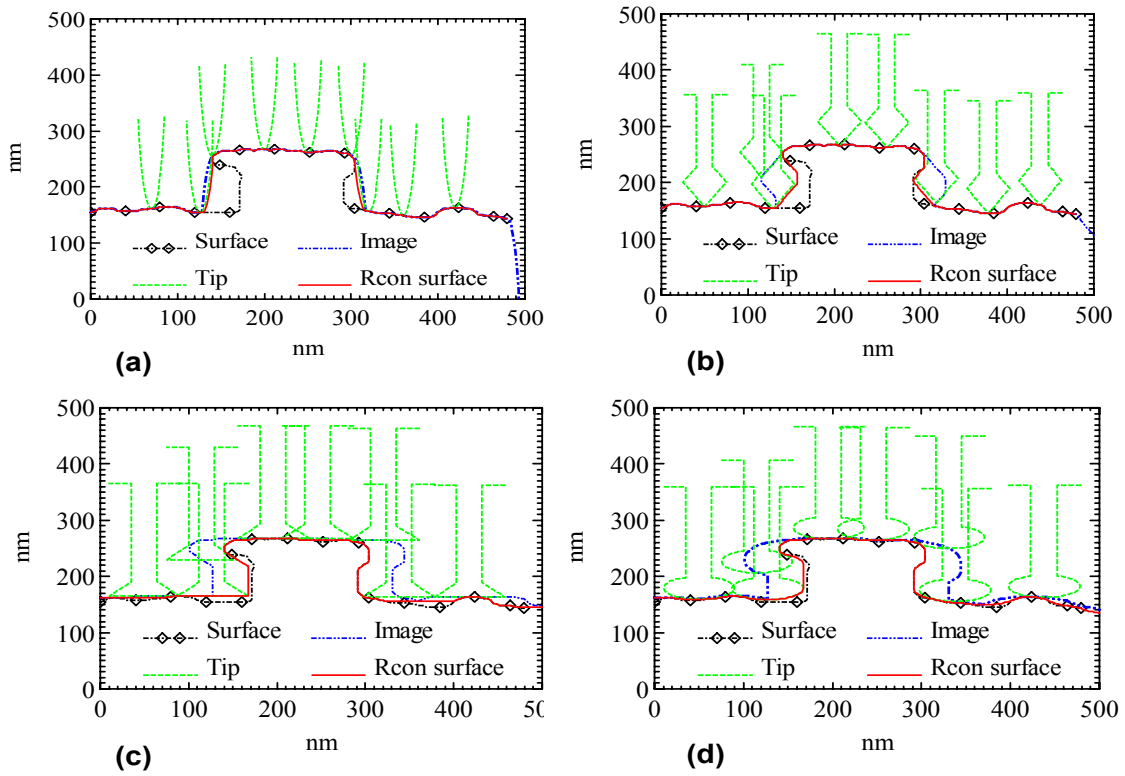


Figure 5 Dilation and erosion on undercut structures by various tips: parabolic tip in (a), three-point tip in (b), sharp flare-shape tip in (c), and elliptical flare-shape tip in (d).

These examples demonstrate the following:

- The conventional tip of a parabolic shape is incapable of fully resolving structures of vertical sidewalls or undercut features since they cannot access the undercut feature or the root of the sidewalls. This is demonstrated in (a) figures in Figure 4 and Figure 5.
- The tip of three-point shape has limited capability in resolving structures of vertical sidewalls and undercut features. For examples, in both examples in (b) figures in Figure 4 and Figure 5, through the three-point probe, we were able to fully recover the top part of the structures, but not the root part of the structures since the probe does not make contact with the roots of the structures.
- The sharp flare shaped tip and elliptical flare-shape tip have much better capability in imaging structures of vertical sidewalls and undercut features. Through the dilation and erosion, we demonstrate that the flare shaped tip and elliptical flare-shape tip can fully recover the specimen surface shape in (c) figures in Figure 4. However, they cannot fully recover the shape for the undercut structure in Figure 5 due to insufficient lateral protrusion. Therefore, the right side of the sidewall is fully recovered and the surface shape of the left sidewall is bounded by the reconstructed surface in this example.

In all the above examples, when the dilation and erosion operation cannot fully recover the specimen surface, the reconstructed surface and the specimen surface are not identical. As expected, the reconstructed surface approximates and correctly bounds the specimen surface.

3.2. 3D structures with reentrant sidewalls and undercut features

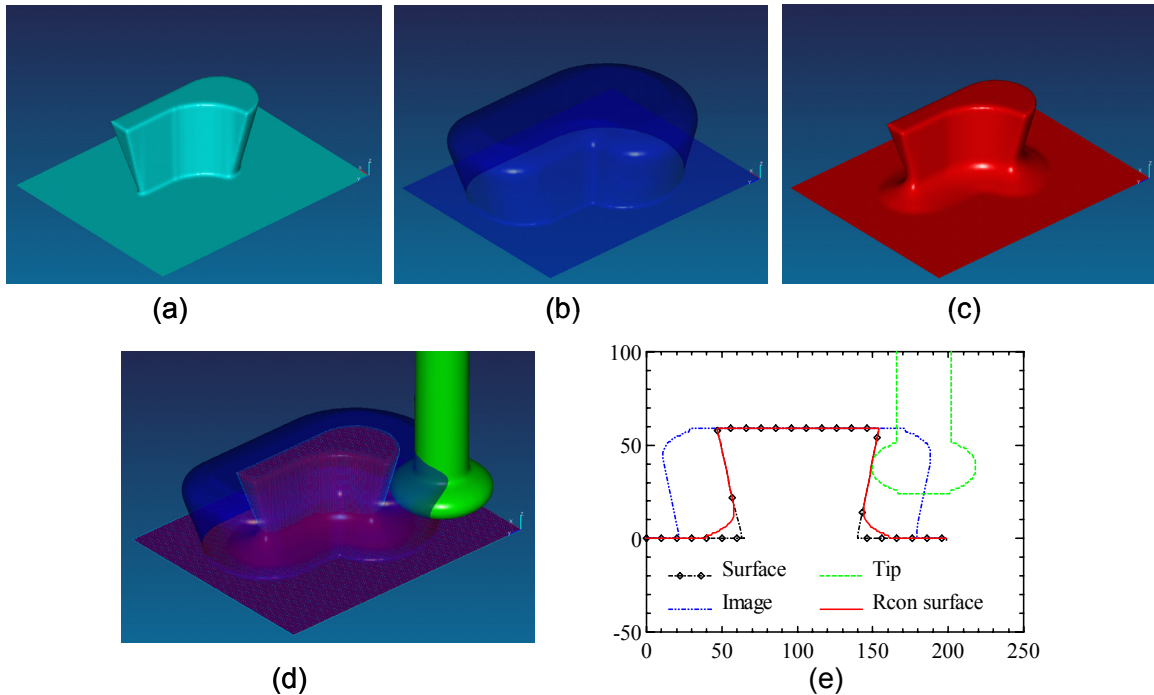


Figure 6 Dilation and erosion on a general 3D undercut structure: (a) specimen structure with undercut, (b) simulated image through dilation, (c) reconstructed surface through erosion, (d) overlay of original surface, simulated image, reconstructed image, and the tip, (e) a cross-sectional view of the overlay.

Example 3 The new software is fully capable of *simulating* AFM images and *reconstructing* specimen surfaces for general 3D structures. We highlight one general 3D undercut structure in Figure 6. Figure 6.a is a 3D structure with undercut on all the sidewalls. Figure 6.b shows the simulated image with dilation and Figure 6.c shows the reconstructed structure with the 3D erosion operation. An overlay of the original structure, simulated AFM image, reconstructed structure and the tip is shown in Figure 6.d to demonstrate

the containment relationships among the image, original structure and the reconstructed structure. Figure 6.e presents a cross-sectional view of such tip-specimen shape interaction. As can be seen from this figure, the reconstructed surface coincides very well with the original structure on the top half and bounds the roots of the original structure. In this example, the surface and image are represented by 160×200 dexels and the tip by 70×70 dexels at a dixel spacing of 1 nm. It takes 34,335 dixel blocks to represent the surface and 7,893 blocks to represent the tip. The time duration for the dilation operation is 11.2 s and the erosion is 10.8 s. The time is recorded from the tests on a PC (Dell Optilex GX520, Pentium® CPU3.40 GHz, 1.99GB RAM).*

3.3. Actual AFM data for structures with undercut features

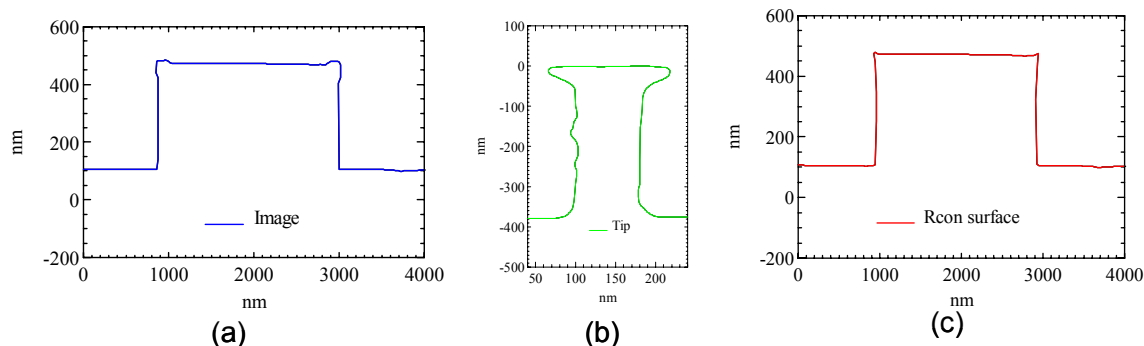


Figure 7 Surface reconstruction from an X3D image of an undercut structure: (a) X3D image, (b) the CDR130SiN tip, and (c) the reconstructed profile through erosion.

Example 4 The new software has also been tested on actual AFM data sets of undercut structures. The data files in this example are in the dixel representation. Even though the actual AFMs capable of bi-directional servo control and imaging undercut features may have the output format as (x, z) pairs, it is not difficult to convert such pairs into the dixel representation through various interpolation methods, such as linear interpolation.

Figure 7.a shows a data acquired from an I2FSR characterizer using a CDR130SiN tip (Figure 7.b) with the Veeco X3D AFM machine. Evident in the data is that the I2FSR characterizer has up-swept edges. The reconstructed surface through erosion reveals just that.

4. CORRECTION OF IMAGING ARTIFACTS: METHOD COMPARISONS

The examples above graphically demonstrate that the new software is capable of simulating AFM imaging of general 2D profiles and reconstructing the surfaces. We can therefore use this software in AFM-based dimensional metrology of nanostructures. The erosion-based surface reconstruction is expected to produce results closer to actual dimensions than the earlier width-subtraction method. Prior research has reported the tip width broadening effect and high order effect [2, 3, 4, 4] at the upper corner and the root of the sidewalls and the bias in the width measurement of the critical dimensions. Quantitative analysis of such bias in width and in sidewall rounded corners was given in [11].

* Commercial equipment is identified in order to specify the measurement procedure. Such identification does not imply recommendation or endorsement by the National Institute of Standards and Technology, nor does it imply that the equipment identified is necessarily the best available for the purpose.

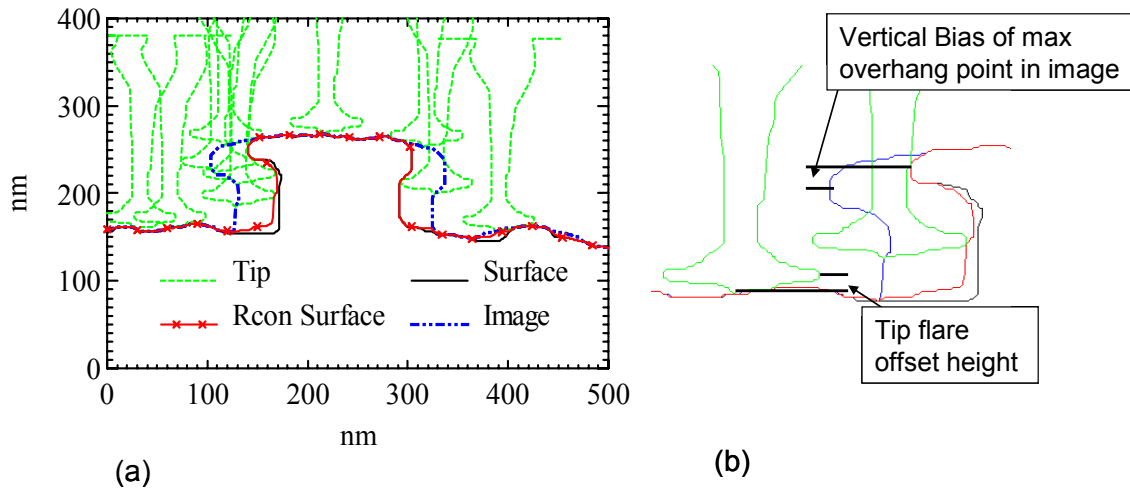


Figure 8 Simulating the bias exhibited in CD-AFM measurement: (a) image simulation and surface reconstruction for an undercut structure, reproduced from Ref. [5] with permission, (b) the tip flare effect and vertical bias.

Example 5 Figure 8 shows an undercut structure imaged by a probe with lateral protrusion. The (b) figure in Figure 8 is a magnified view of the vertical bias at the maximum overhang position induced by the tip flare offset height. This is consistent with the high order effect pointed out in [2, 3].

This demonstrates that the dixel-based software can accurately reproduce the high order effect and the results are also conformal to the analytical results given in [4].

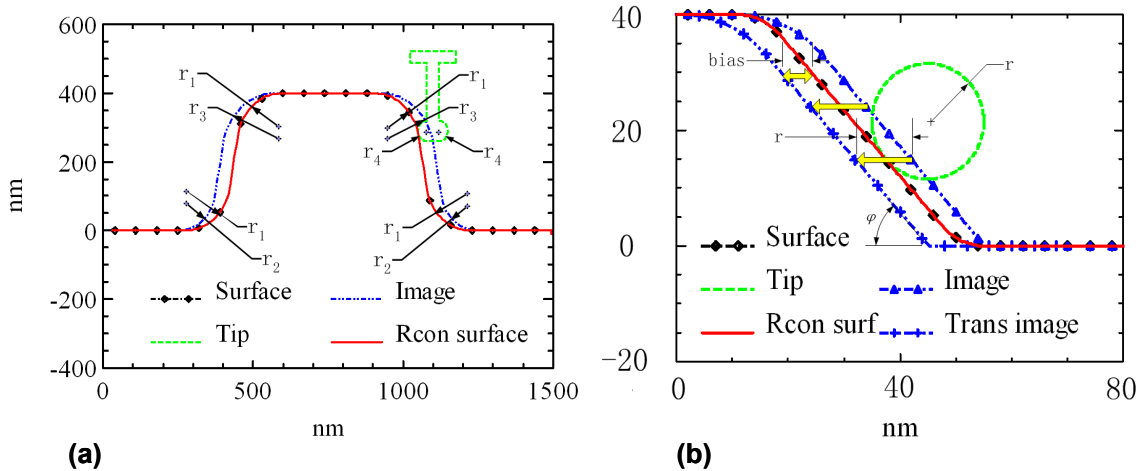


Figure 9 Quantitative evaluation of probe-induced measurement bias: (a) tip-effect on the round corner, (b) tip-effect on the structural width with sloped sidewalls.

Example 6 Figure 9 provides examples of quantitative evaluation of probe-induced measurement bias on the round corners and on the structural width with sloped sidewalls.

If the tip radius is r_4 and the radii of the top and bottom round corners in the surface are both r_1 , then the radii of the top corner of the image is $r_3 = r_1 + r_4$ and the radius of the bottom corner is $r_2 = r_1 - r_4$ [11] In Figure 9.a, $r_1 = 150$ nm and $r_4 = 30$ nm. Therefore, the expected $r_3 = 180$ nm and $r_2 = 120$ nm. In the dixel calculation, using discretized versions of the image, sample, and tip, dilation yields radii at the top

and bottom corners of (180.0 ± 0.3) nm and (130 ± 0.8) nm. These compare favorably with the analytical result.

If the structure has the same slope for the two sidewalls, as shown in Figure 9.b, the tip radius induced width bias is expected to be $r[1 - \tan(\varphi/2)]$ [4], where φ is the angle of the sidewall with respect to the substrate (i.e., $\varphi = 90^\circ$ is a vertical sidewall). In our example above, $r = 10$ nm, and $\varphi = 48.6^\circ$. Our measured bias differs from the expected one by less than 6 pm when the dixel resolution is 300/nm. This small difference can be attributed to the discreteness of the approximation (the difference is smaller when dixel resolution is higher), and is small compared to expected measurement errors from other sources.

These examples demonstrate that our implementation gives results consistent with the analytical analysis and that common tip effects reported in the literature, such as tip width broadening and the so-called higher order effect can be effectively removed using the erosion operation.

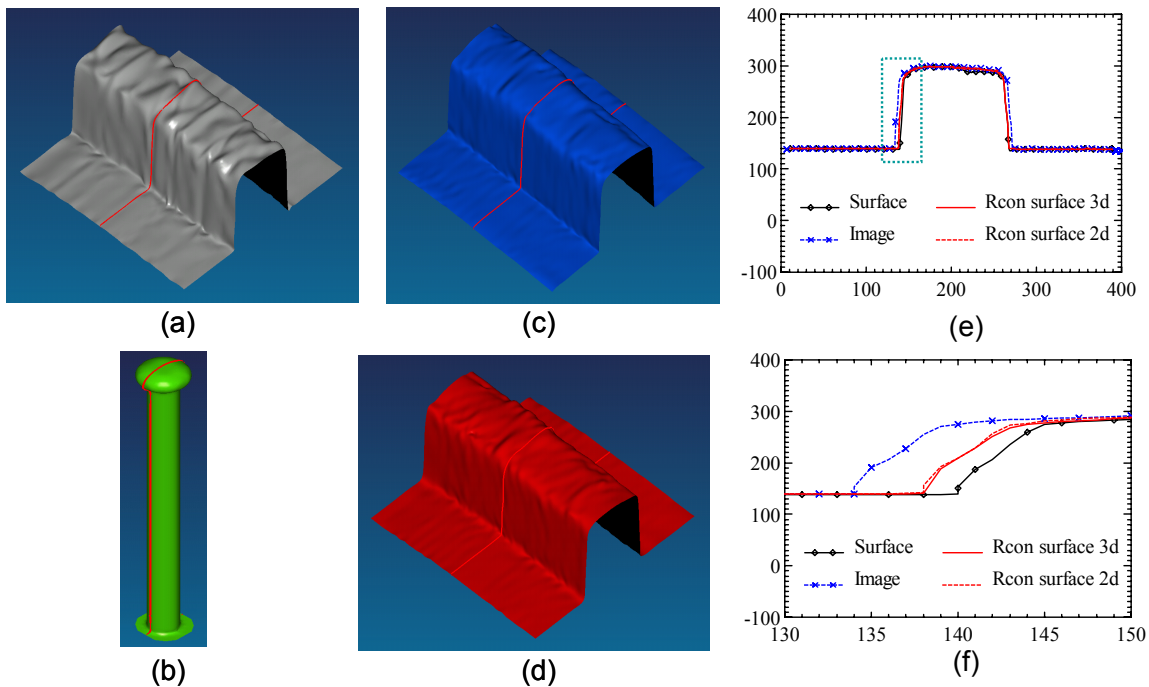


Figure 10 3D Reconstruction simulation on a set of SXM data of vertical sidewalls: (a) SXM data, (b) reversed tip, (c) image through dilation, (d) 3D reconstructed surface through erosion, (e) comparison of 2D erosion and 3D erosion, (f) magnified view of the comparison.

Example 7 Figure 10 shows a 3D reconstruction simulation based on 40 measured profiles of a near-vertical structures. The data was acquired using NIST’s SXM AFM machine. Figure 10.a shows 3D surface rendered from the 40 profiles. The use of actual imaged AFM data as a simulated specimen surface is to increase the realism of the simulation. Figure 10.b presents a reversed tip. Through dilation by the 3D tip, we obtain the simulated image in Figure 10.c. Through erosion by the 3D tip, we obtain the reconstructed surface in Figure 10.d. In this example, the surface and image are represented by 400×40 dexels and the tip by 10×10 dexels. It takes 16,124 dixel blocks to represent the surface and 169 dixel blocks to represent the tip. The time duration for the dilation and erosion are both approximately 0.94 s.

An erosion simulation can also be done for each of the 2D profile alone, as is typically done in today’s practice. Figure 10.e and Figure 10.f (the magnified view) demonstrates the difference between full 3D erosion and a 2D erosion of one profile drawn from the middle section of the 3D object (as indicated in Figure 10.a and Figure 10.d). The 2D and 3D reconstruction results differ slightly, with 2D one forming an upper bound on the full 3D one as expected. The reason for the difference is that on a rough-edged line the

image along a particular profile (e.g., along the x direction at constant y) may have been produced by contact of the tip with the sample at a point not in the profile (i.e., at some different y value). A 2D reconstruction cannot account for this effect. The magnitude of this effect is expected to depend upon the edge roughness, and will be largest when the roughness wavelengths are comparable to or smaller than the tip size. Although the difference appears to be small in this illustration, its smallness may be illusory—an artifact of the way the example was constructed. This particular “sample” already includes dilation by the SXM tip used to acquire the image, and that dilation will have washed out much of the roughness that might otherwise produce such differences between 2D and 3D reconstructions. This is illustrated in the next example.

Example 8 A line with simulated waviness (cylinders with approximate radius of 350 nm, with axes perpendicular to the substrate and with edges overlapping somewhat) is shown in Figure 11. When imaged by a probe of radius 200 nm an image profile across the midsection of the line is the outermost line shown in Figure 11b. A 2D erosion leads to the outer of the two dashed reconstruction profiles, 3D erosion to the inner one. The 3D reconstruction retains negligible bias relative to the true surface profile at half the full height, while the 2D reconstruction retains a bias of 56 nm.

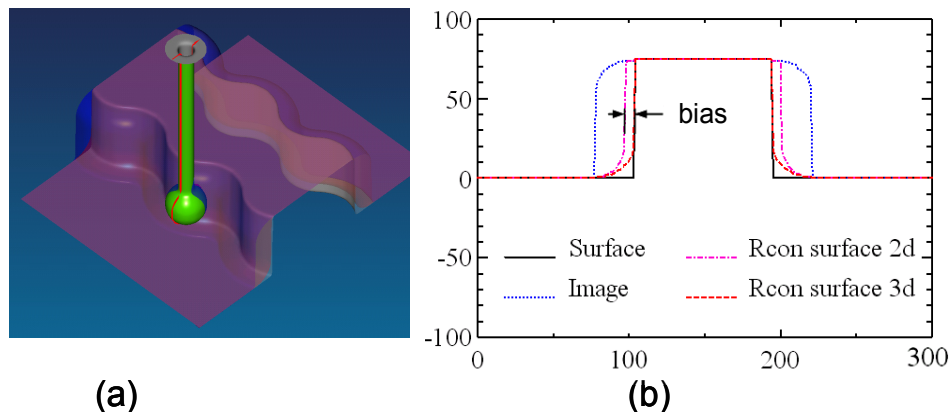


Figure 11 Full 3D erosion corrects some bias that remains uncorrected by 2D erosion in current practice: a) a line with simulated roughness, b) bias due to 2D erosion.

5. CONCLUSIONS

This paper presents applications of a new mathematical morphology method for AFM-based image simulation and surface reconstruction that is applicable to general 3D structures with vertical sidewalls or undercut features. The new method is based on a dixel representation, which represents a 3D object in a rectangular array with each array containing a list of object heights.

Due to the underlying dixel representation, the software is able to model tip-specimen shape interaction for general 3D structures and is capable of dilation and erosion operations for 3D objects.

Various examples in this paper illustrate the following capabilities of the dixel-based approach:

- capable of representing complex 3D structures with vertical sidewalls and undercut features
- capable of simulating AFM images of 3D objects and reconstructing the surfaces from the images
- capable of removing various tip-induced artifacts using the erosion operations.

These examples also demonstrate that the *erosion*-based method produces reconstructed surface better than the simple *width subtraction* in critical dimensional measurement applications.

6. ACKNOWLEDGEMENT

We are grateful for the X3D data provided by Greg Dahlen from Veeco Instruments.

REFERENCES:

1. Y. Martin and H. K. Wickramasinghe, "Method for imaging sidewalls by atomic force microscopy," *Applied Physics Letter*, Vol. **64**, pp. 2498-2500 (1994).
2. N. G. Orji and R. G. Dixon "Higher order tip effects in traceable CD-AFM-based linewidth measurements". *Meas. Sci. Technol.* **18**, pp. 448-455 (2007).
3. N. G. Orji, R. G. Dixon, A. Martinez, B. D. Bunday, J. A. Allgair, T. V. Vorburger "Progress on Implementation of a CD-AFM-Based Reference Measurement System," *Journal of Micro/Nanolithography, MEMS and MOEMS*, to be published.
4. G. Dahlen, M. Osborn, N. Okulan, W. Foreman, A. Chand, and J. Foucher, "Tip characterization and surface reconstruction of complex structures with critical dimension atomic force microscopy," *J. Vac. Sci. Technol.* **B23**, pp. 2297-2303 (2005).
5. X. Qian and J. S. Villarrubia, "General three-dimensional image simulation and surface reconstruction in scanning probe microscopy using a dixel representation," *Ultramicroscopy*, 2007, in press.
6. J. S. Villarrubia, "Algorithms for Scanned Probe Microscope Image Simulation, Surface Reconstruction, and Tip Estimation," *J. Res. Nat. Inst. Stand. Technol.* **102**, pp. 425 - 454, (1997), <http://nvl.nist.gov/pub/nistpubs/jres/102/4/j24vil.pdf>
7. J. S. Villarrubia, "Morphological estimation of tip geometry for scanned probe microscopy," *Surf. Sci.* **321**, 287 (1994).
8. E. E. Hartquist, J. P. Menon, K. Suresh, H. B. Voelcker, and J. Zagajac, "A computing strategy for applications involving offsets, sweeps, and Minkowski operations," *Computer-Aided Design* **31**, pp. 175- 183 (1999).
9. R. M. Haralick, S. R. Sternberg, and X. Zhuang, in *IEEE Transactions on Pattern Analysis and machine Intelligence*, PAMI-9, pp. 532-550 (1987).
10. D. Nyssonen, L. Landstein, and E. Coombs "Two-dimensional atomic force microprobe trench metrology system," *J. Vac. Sci. Technol. B* **9**, pp. 3612- 3616 (1991).
11. G. Dahlen, M. Osborn, N.-C. Liu, R. Jain, W. Foreman, and J. R. Osborne, "Critical Dimension AFM tip characterization and image reconstruction applied to the 45 nm node," *Proc. SPIE* **6152**, pp. 61522R-1-11 (2006).